PNAS RESEARCH ARTICLE | ENVIRONMENTAL SCIENCES OPEN ACCESS

Climate forcing controls on carbon terrestrial fluxes during shale weathering

Lucien Stolze[a,1], Bhavna Arora[a], Dipankar Dwivedi[a], Carl I. Steefel[a], Toshiyuki Bandai[a], Yuxin Wu[a], and Peter Nico[a]

Edited by Peter Kelemen, Lamont-Doherty Earth Observatory, Palisades, NY; received January 6, 2024; accepted May 13, 2024

Climate influences near-surface biogeochemical processes and thereby determines the partitioning of carbon dioxide (CO_2) in shale, and yet the controls on carbon (C) weathering fluxes remain poorly constrained. Using a dataset that characterizes biogeochemical responses to climate forcing in shale regolith, we implement a numerical model that describes the effects of water infiltration events, gas exchange, and temperature fluctuations on soil respiration and mineral weathering at a seasonal timescale. Our modeling approach allows us to quantitatively disentangle the controls of transient climate forcing and biogeochemical mechanisms on C partitioning. We find that ~3% of soil CO_2 (1.02 mol C/m^2/y) is exported to the subsurface during large infiltration events. Here, net atmospheric CO_2 drawdown primarily occurs during spring snowmelt, governs the aqueous C exports (61%), and exceeds the CO_2 flux generated by pyrite and petrogenic organic matter oxidation (~0.2 mol C/m^2/y). We show that shale CO_2 consumption results from the temporal coupling between soil microbial respiration and carbonate weathering. This coupling is driven by the impacts of hydrologic fluctuations on fresh organic matter availability and CO_2 transport to the weathering front. Diffusion-limited transport of gases under transient hydrological conditions exerts an important control on $CO_{2(g)}$ egress patterns and thus must be considered when inferring soil CO_2 drawdown from the gas phase composition. Our findings emphasize the importance of seasonal climate forcing in shaping the net contribution of shale weathering to terrestrial C fluxes and suggest that warmer conditions could reduce the potential for shale weathering to act as a CO_2 sink.

carbon cycling | soil respiration | shale weathering | climate forcing | multiphase transport

Significance

Shale weathering represents a key component of the global carbon (C) cycle by producing carbon dioxide (CO_2) through oxidation reactions and consuming CO_2 via carbonate weathering. In this contribution, we investigate how climate forcing controls the partitioning of C fluxes associated with shale weathering by implementing a numerical model that simulates the interactions between soil respiration and mineral reactions under transient conditions. We find that large rewetting events enhance carbonate weathering by stimulating soil microbial respiration and controlling the delivery of carbonic acid at depth. This mechanism is important as it represents the main pathway for atmospheric CO_2 sequestration in the subsurface. Our findings indicate that the potential of shale weathering to act as a CO_2 sink will be altered by climate change.

Shales significantly contribute to terrestrial carbon (C) fluxes because they represent an important reservoir of carbon stored in the form of petrogenic organic matter (OM) and carbonate minerals that can be mobilized through weathering (1). Shale weathering occurs when rocks become exposed to atmospheric conditions through tectonic uplift and/or erosion. Under such conditions, strong chemical gradients extend between the Earth's oxic surface and the bedrock at depth characterized by reducing conditions. The mixing of reactants at this interface through gas exchange and meteoric water infiltration stimulates a variety of biological and geochemical processes leading to the depletion of shale-associated OM, carbonate, and sulfide minerals composing the parent rock (2, 3). While the oxidation of petrogenic OM [also referred to as georespiration (4)] represents a source of CO_2 to the atmosphere (1, 5), carbonate and silicate mineral dissolution driven by respiration processes and/or atmospheric CO_2 transfers C to the subsurface (6–10). In particular, the interaction between soil respiration and carbonate weathering is recognized as an important mechanism of atmospheric CO_2 regulation at the decadal timescale and a source of base cations from land to ocean (11, 12).

Climate forcing plays a key role for weathering as variations in temperature and hydrological conditions modulate ecosystem respiration response (13), influence the thermodynamics of the carbonate system (11) and the kinetics of biogeochemical reactions (14–16), and determine the propagation of reactive chemical species in the subsurface (17). For instance, enhanced CO_2 drawdown from soil to bedrock as well as dissolved inorganic carbon (DIC) exports have been evidenced during periods combining soil respiration and infiltration events (7–9). Despite the implications of shale weathering for freshwater quality (18, 19) and Earth's climate (20), the accurate quantification of C fluxes in the near land surface (or Critical Zone) and, in particular, of the balance between CO_2 produced and consumed by weathering remains a daunting challenge. This limitation is in part the result of i) the dominance of carbon cycling in soil which can overprint the contribution of weathering processes to C fluxes (21), ii) the multiple geochemical controls on pH and CO_2 that simultaneously influence the carbonate system [i.e., georespiration, oxidation of sulfide minerals, weathering of carbonate and silicate minerals (e.g., refs. 4,

Author affiliations: [a]Earth and Environmental Sciences Area, Lawrence Berkeley National Laboratory, Berkeley, CA 94720

Author contributions: L.S., B.A., D.D., C.I.S., and P.N. designed research; L.S., C.I.S., and T.B. performed research; Y.W. analyzed data; and L.S. wrote the paper.

The authors declare no competing interest.

This article is a PNAS Direct Submission.

[1]To whom correspondence may be addressed. Email: lstolze@lbl.gov.

This article contains supporting information online at https://www.pnas.org/lookup/suppl/doi:10.1073/pnas.2400230121/-/DCSupplemental.

Published June 24, 2024.

15, 22, and 23)], and iii) the multifaceted controls of climate forcing. In particular, due to the sensitivity of biogeochemical processes to hydrochemical and physical conditions, climate forcing results in distinct seasonal variations in soil heterotrophic and root autotrophic respirations (13), activation and/or inhibition of weathering reactions through increased availability and/or depletion of reactants (22), as well as positive and negative responses of the reactions to temperature.

Unraveling the mechanisms that control the hydrogeochemical fluxes of carbon between the atmosphere and the subsurface requires a multidisciplinary approach that integrates the description of partially saturated flow, transport of chemical species through the gas and aqueous phases, water–rock interaction, and soil biological processes. To this end, process-based reactive transport models are key for performing physics-based mass balance calculations and for quantitatively interpreting the complex interplay between physical, chemical, and biological processes at critical interfaces (24, 25). Current modeling approaches focused on weathering typically assume steady state and fully saturated flow conditions and/or adopt simplified representations of the hydrogeochemical conditions (26, 27). Furthermore, models integrating both descriptions of ecosystem C cycling and weathering-derived C fluxes remain rare (28) despite the intertwined effects of these processes on global C cycling. To our knowledge, a rigorous assessment of the carbon mass balance that integrates all key components and considers the inherently transient aspect of ecosystem respiration and weathering as well as the interplay between the different compartments composing the subsurface/atmosphere interface (atmosphere, soil, and saprolite) is missing.

This study explores how seasonal variations in climate forcing (precipitation, heat transfer, and gas exchange) shape the partitioning of inorganic C fluxes in the regolith of carbonaceous shale. Here, the regolith refers to the zone overlying fresh bedrock and encompassing the soil and weathered rock, which is characterized by intense biological activity, rock weathering, and hydrogeochemical exchange of reactants both in the liquid and gaseous phases. Based on a field dataset collected at a well-characterized field site of a high elevation watershed in Colorado and characterizing the spatial variability and temporal change in biogeochemical conditions in the near-surface of shale, we develop a data-driven physics-based model describing the dynamic mass transfer of carbon across the regolith. The implementation of the numerical model is constrained and validated by the integration of depth-discretized measurements on temporal change in gas and aqueous phase composition as well as the characterization of the spatial distribution of solid phases. Using our model, we provide a quantitative interpretation of the fluxes of carbon associated with the weathering of shale and the multifaceted controls of external forcing. By simultaneously describing soil respiration and mineral reaction and their combined effects on C fluxes over a continuum and under transient conditions, our modeling framework allows us to study how the rapid cycling of carbon in soil is linked to long-term carbon fluxes associated with weathering. Fig. 1 presents a visual representation of the conceptual framework for the proposed approach including the key multiphase and biogeochemical processes controlling the mobilization, transport, and sequestration of carbon.

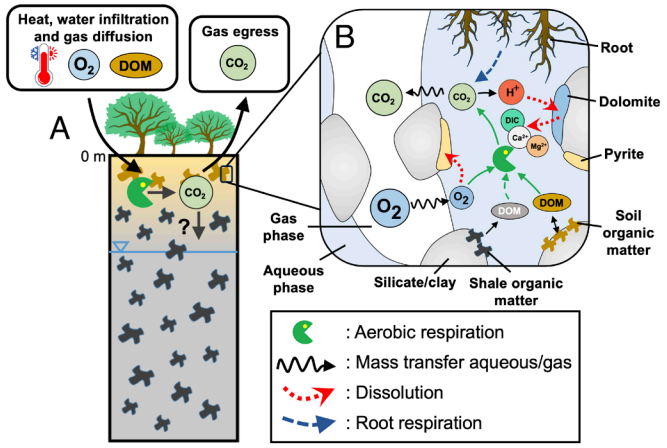

Fig. 1. Schematic illustration of the coupling between soil respiration and shale weathering and the associated biogeochemical cycling of carbon. (*A*) Biogeochemical reactions in the regolith are driven by i) the exchange of gases at the subsurface/atmosphere interface, ii) the infiltration of meteoric water mobilizing labile soil organic matter, iii) the presence of plants, which mobilize or take up solutes via root respiration and transpiration, iv) the distribution of fossil shale-associated organic matter (i.e., dominant below the soil horizon; 1 m below the ground surface at the considered field site), v) the microbes metabolizing chemical compounds to gain energy (catabolic pathway) and growth (anabolic pathway), and vi) the minerals which undergo precipitation/dissolution reactions. Furthermore, variations in air temperature influence the biogeochemical processes in the near-surface. The biogenic CO_2 produced in soil is emitted to the atmosphere via gas diffusion or sequestered in the subsurface via advective transport and biogeochemical processes. (*B*) Oxygen diffuses from the gas phase to the aqueous phase, where it drives the mineralization of organic matter and the oxidative dissolution of pyrite. Part of the biogenic CO_2 generated by microbial respiration and root respiration returns to the gas phase. Acidification of the pore water due to carbonic and/or sulfuric acid drives the dissolution of carbonate minerals (dolomite in this case).

Results

Integration of a Multiphase Dataset in a Unified Modeling Framework. To develop the proposed modeling framework, we consider a well-instrumented transect located in the East River watershed (*SI Appendix*, Fig. S1), a snow-dominated pristine mountainous watershed within the Upper Colorado River basin (29). The transect is underlain by Mancos shale, a Cretaceous marine formation that is broadly distributed in the Western United States. The vegetation consists in grasses, forbs, and shrubs representative of the regional lower montane life zone. At the catchment scale, the coupling between snowmelt, biological processes, and shale weathering exerts a strong control on the hydrogeochemical exports to the river system (22, 30, 31). Three monitoring wells (PLM1-3) were drilled to monitor the hydrogeological, geochemical, and hydrochemical conditions.

At our site, the shale has a total organic carbon (TOC) content of 1.25 wt% and is enriched with dolomite (13.70 wt%) and pyrite (0.90 wt%; *SI Appendix*, Figs. S1 and S2). Depth-resolved solid sampling and analysis show that the regolith extends to a depth of three to four meters, which corresponds to the maximum depth of the water table. The regolith is characterized by significant depletion of dolomite and pyrite and precipitation of secondary minerals (i.e., calcite and goethite). Concentrations of the other minerals composing the parent rock (i.e., silicate, clay) are spatially homogeneous showing limited weathering (*SI Appendix*, Fig. S2). The soil horizon has a thickness of about 1 m and presents significantly higher TOC content and C/N ratio compared to that of the saprolite and the parent rock. Such a spatial distribution is due to the accumulation of litter/plant-derived OM (here referred to as soil OM) having a significantly different composition than the shale-associated OM (32). Biogeochemical response to climate forcing was characterized in the field using i) water and gas samples collected and analyzed at weekly to monthly time intervals from depth-discretized lysimeters (33), ii) daily measurements of $CO_{2(g)}$ flux from the soil to the atmosphere (this study), and iii) the seasonal change in soil microbial biomass reported by Sorensen et al. (34). Fig. 2 presents an

overview of the hydrogeochemical conditions and the exchange of reactants at the soil/atmosphere interface.

We use this comprehensive dataset to build the process-based model and to constrain the mass balance calculations directly on measurements performed in the aqueous, gas, and solid phases. Specifically, we integrate the observed spatial distribution of solid phases (i.e., mineral and organic matter concentrations) and time-dependent changes in external forcing (i.e., local snowmelt drainage conditions, evapotranspiration rates, and depth discretized temperature fluctuations) into the numerical model. The model mathematically describes the fluid phase dynamics of partially saturated flow, the mass transfer of chemical species between the liquid and gaseous phases, the transport of aqueous and gaseous species, and the biogeochemical processes occurring in the soil and the saprolite. Comparison between measurements and simulation results presented in Fig. 2 shows that our approach allows us to capture i) the spatial distribution of the solutes (Fig. 2 *A*–*D*; $R^2 > 0.5$), ii) the temporal evolution of the $CO_{2(g)}$ concentration in the porous matrix (Fig. 2*D*; $R^2 = 0.3$), iii) the transient change in $CO_{2(g)}$ efflux (Fig. 2*G*; $R^2 = 0.83$), and iv) the temporal evolution of the microbial biomass concentration (Fig. 2*I*; $R^2 = 0.93$).

Measurements and simulation results highlight strong differences in the hydrogeochemical conditions of the soil and the saprolite horizons over the vertical extent of the regolith. In particular, concentrations of DIC and base cations released from carbonate weathering sharply increase below a depth of 1 m (i.e., average DIC, Mg^{2+}, and Ca^{2+} concentrations are 1.46, 0.27, and 0.50 mM in soil and 4.30, 1.01, and 1.91 mM in the saprolite, respectively; Fig. 2 *A*–*C*). This heterogeneous distribution reflects the lower influence of carbonate weathering on the hydrogeochemical conditions in the soil compared to that in the saprolite due to depletion of dolomite in the top 1 m. Furthermore, the DIC and base cations concentrations remain remarkably steady (Fig. 2 *A*–*C*). This chemostatic behavior suggests the occurrence of rapid change in the biogeochemical reaction rates that allow the system to overcome dilution effects during large infiltration events induced by snowmelt and significant rainfall (Fig. 2*F*).

Regarding the chemical composition of the gas phase, the $CO_{2(g)}$ concentration in the regolith (3,144 ppm on average; Fig. 2*D*) is significantly higher than the atmospheric $CO_{2(g)}$ concentration (211 ppm at the altitude of the field site) due to the biological processes generating CO_2 (i.e., root respiration, heterotrophic microbial respiration, and georespiration). Although CO_2 concentration in the gas phase decreases toward the top of the profile because of the mixing with atmospheric air, a clear seasonal increase in CO_2 gas concentration occurs within the soil horizon during snowmelt (Fig. 2*D*) indicating strong transient biogeochemical responses to climatic events [i.e., hot moments (35)]. The model shows that this increase is accompanied by a decrease in soil pH from alkaline conditions (pH ~ 8.5) to circumneutral conditions (pH ~ 6.5; Fig. 2*E*).

Significant CO_2 production in soil and biogeochemical hot moments are further evidenced by the temporal evolution of $CO_{2(g)}$ fluxes between the soil and the atmosphere (Fig. 2*G*) and the variation in soil microbial biomass (Fig. 2*I*). In fact, both the measured and model-computed $CO_{2(g)}$ efflux significantly increases upon snowmelt, reaching a maximum of 85.55 mol C/m^2/*y* in June. Following this peak, the $CO_{2(g)}$ efflux decreases as the soil dries out and remains constant throughout fall and winter when water saturation and

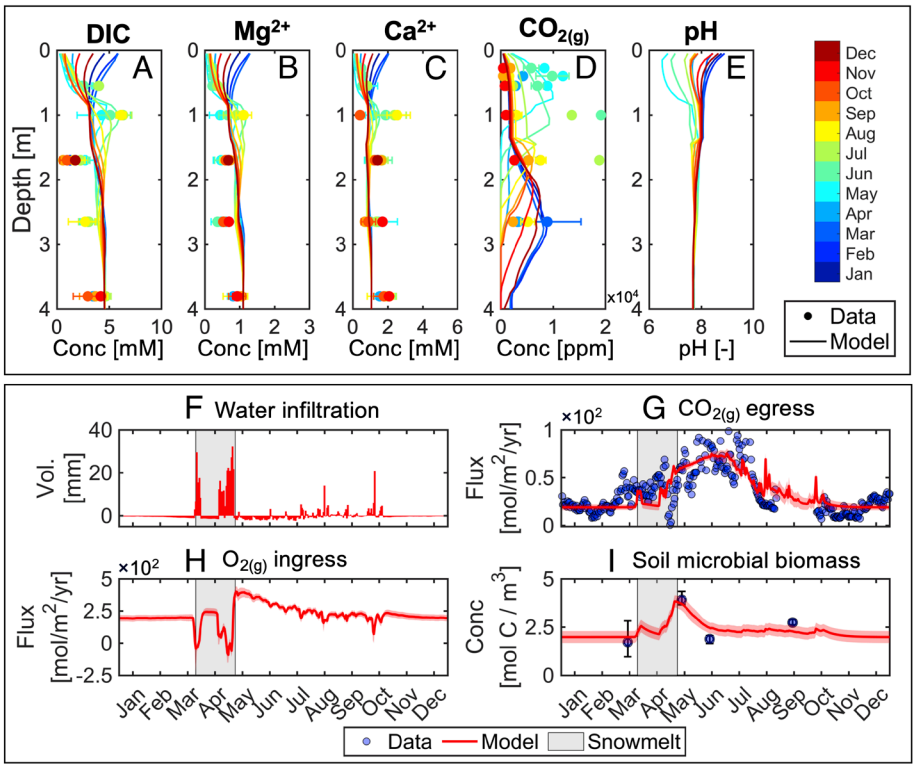

Fig. 2. Comparison between measured and simulated temporal evolution of the hydrogeochemical conditions in the regolith, exchange of reactants between the atmosphere and the subsurface, and soil microbial biomass. (*A*–*E*) Spatial distribution of aqueous and gas concentrations of carbon and base cations in PLM2. Measurements are shown as monthly average for clarity with error bars indicating the minimum and maximum concentrations. Results for the two other PLM wells are presented in *SI Appendix*. (*F*) Water infiltration time series. (*G* and *H*) Temporal evolution of the gas fluxes at the soil/atmosphere interface. (*I*) Temporal change in soil microbial biomass concentration. The error bars in panel (*I*) show the total range of the field measurements. Symbols represent the measured field data, and solid lines represent the results of the process-based model.

biological activity are lowest (minimum is 13.12 mol C/m^2/y). Although the $CO_{2(g)}$ efflux from the soil surface aggregates the contribution of multiple biogeochemical processes releasing and consuming CO_2 (e.g., soil respiration and carbonate mineral weathering, respectively), such a large increase associated with pulse-wetting events generally indicates an increase in biological reaction rates, a phenomenon known as the Birch effect (36). The onset of the large $CO_{2(g)}$ efflux during snowmelt coincides with an increase in soil microbial biomass (Fig. 2*I*), suggesting that heterotrophic respiration contributes to the temporal trends of the $CO_{2(g)}$ emissions. Furthermore, the relatively smooth temporal evolution of soil microbial biomass and the steady albeit lower $CO_{2(g)}$ efflux during winter indicates that microbial activity in soil is maintained under the snow cover as snowpack insulation prevents the soil from freezing (34). This is in agreement with previous observations made in snow-covered soils in subalpine environments (37, 38).

Spatiotemporal Distribution of Respiration and Weathering Processes. We use the results of the numerical simulations to characterize and compare the spatial distribution and temporal variations of the respiration and weathering processes. Fig. 3 displays the temporal change in water saturation and temperature occurring throughout the year and the resulting evolution of the biogeochemical reaction rates at three depth intervals within the soil and the saprolite: [0 to 0.5] m, [1 to 1.5] m, and [2 to 2.5 m].

Fig. 3*A* shows that water saturation progressively increases with depth and undergoes strong variations above 2 m by peaking as a response to snowmelt and receding during summer. In contrast, subsurface temperature shows smoother fluctuation with maximum and minimum values observed in summer and winter, respectively. The magnitude of the temperature fluctuation decreases with depth due to the thermal conductivity of the porous matrix.

The simulation results indicate that respiration is dominant in the shallowest part of the subsurface (i.e., [0 to 0.5] m) in contrast to mineral weathering reactions that are strongest below the soil horizon (e.g., carbonate weathering is highest within the depth interval [1 to 1.5] m). The results also highlight the dominant roles of soil heterotrophic respiration (Fig. 3*C*) and root respiration (Fig. 3*D*) in controlling the temporal change in $CO_{2(g)}$ efflux observed at the soil/atmosphere interface as their rates are significantly higher than that of other biogeochemical processes (e.g., Fig. 3 *E*–*H*). In particular, the temporal evolution of the rate of heterotrophic respiration is characterized by a sharp peak that occurs during snowmelt (average and maximum in the soil are 31.93 and 90.57 mol C/m^3/y, respectively). The response of heterotrophic respiration to snowmelt is immediate despite the limited gas diffusion of oxygen during high infiltration events (Fig. 2 *F* and *H*). In fact, this increase is caused by the enhanced availability of labile dissolved organic matter (DOM) to microorganisms under higher water saturation conditions (39) and, to a lesser extent, the leaching of litter DOM from the top soil (*SI Appendix*, Fig. S11). In addition, the dissolved oxygen transported via advection by infiltration of snowmelt enhances the decomposition of DOM (*SI Appendix*, Fig. S11). The simulated heterotrophic respiration rate is at a maximum at the end of snowmelt because both microbial biomass concentration (Fig. 2*I*) and the availability of substrates (i.e., both O_2 and labile soil DOM; *SI Appendix*, Fig. S11) are highest at this time.

In contrast to microbial respiration, the response of root respiration is more progressive and lags behind snowmelt (Fig. 3*D*). Such difference results from a higher sensitivity of root respiration

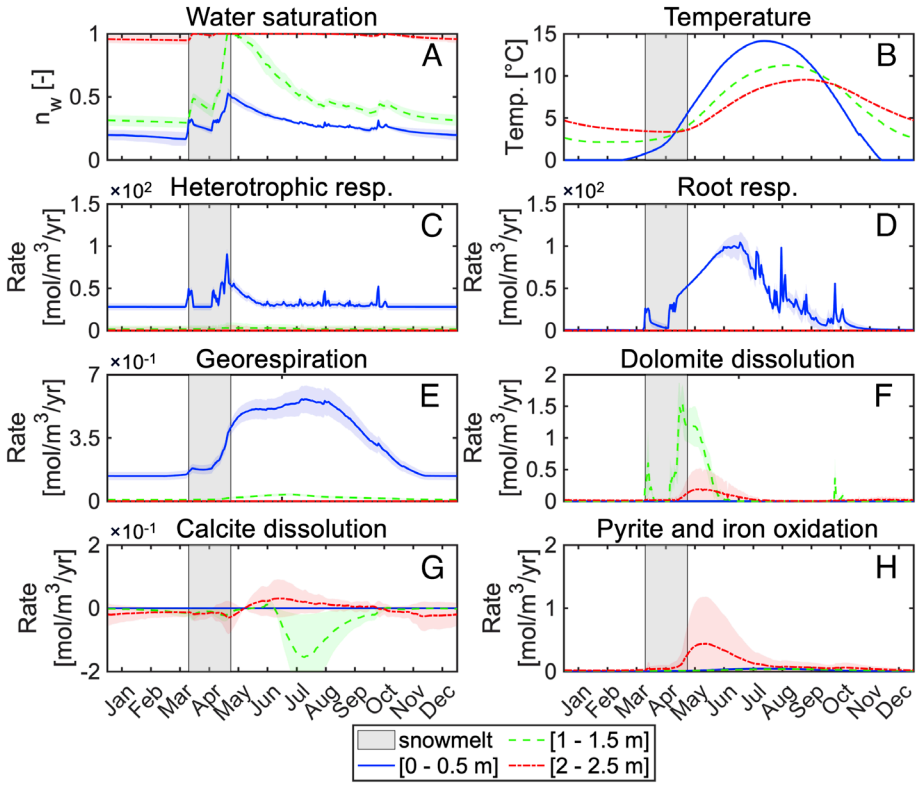

Fig. 3. Simulated temporal change in physical conditions and biogeochemical reaction rates at three locations of the regolith. Georespiration shown in panel (*E*) refers to the oxidation of petrogenic organic matter associated with shale (4). Panel (*H*) shows the rate of total proton release during the oxidation of pyrite, the oxidation of ferrous iron, and the precipitation of goethite (see reactions in Table 1). The lines and shaded areas show the average and SD of the biogeochemical reaction rates, respectively, that were calculated using the simulation results in the three PLM wells. Simulation results for each observation well are presented in *SI Appendix*.

to temperature as shown by their similar trends (Fig. 3 *B* and *D*) and the result of an additional simulation in which the temperature was assumed constant (*SI Appendix*, Fig. S16). Root respiration reaches a maximum in June during the growing season when it dominates the total soil respiration (average and maximum of root respiration in the soil are 27.34 and 104.37 mol C/m^3/y, respectively). We acknowledge that above-ground factors such as photosynthetically active radiation can affect root respiration, but it is beyond the scope of this study to explicitly account for these factors in our model. Furthermore, the simulated alternation between heterotrophic and root respiration at a seasonal timescale, characterized by a rapid response of microbial respiration to infiltration events after a dry period and followed by a more progressive response of autotrophic soil respiration, corroborates previous studies showing similar response for different types of ecosystems (e.g., refs. 4 and 13). Such similarity provides confidence about the model's ability to simulate the respective dynamics of heterotrophic and root respiration. The rainfall events occurring during the summer monsoon (Fig. 2*F*) lead to short peaks in soil respiration (Fig. 3 *C* and *D*) but do not impact the overall seasonal trend since rain events have only a limited effect on the soil water saturation in comparison to snowmelt (Fig. 3*A*). Soil respiration reaches a minimum in winter in the absence of recharge and lower temperature that reduces biological activity.

Because of the higher recalcitrance of shale-associated OM compared to soil OM, soil respiration typically overprints the effect of shale-associated OM oxidation on subsurface CO_2 concentrations (3, 4, 21). Here, we parameterize the rate of georespiration using a recent estimate of CO_2 flux associated with shale OM oxidation made in the East River catchment [2.1×10^{-1} mol C/m^2/y (40)]. Simulation results displayed in Fig. 3*E* show that georespiration is highest in the top first meter due to the prevailing oxic conditions but remains two orders of magnitude lower than that of soil respiration processes (Fig. 3 *C* and *D*). Moreover, higher summer temperature induces a significant response in the rate of georespiration increasing from 2.1×10^{-1} to 5.6×10^{-1} mol C/m^3/y between March and July (Fig. 3*E*). Despite the use of equal Q_{10} values to simulate the temperature dependency of microbial respiration (i.e., 2.1) (15, 41), such a response was not simulated for soil heterotrophic respiration (Fig. 3*C*) because of the difference in rate-limiting factors of these reactions. In the case of soil heterotrophic respiration, the oxidation rate is primarily controlled by the substrate availability as soil DOM is mobilized during infiltration events and rapidly degraded. In contrast, the release of shale-derived DOM was simulated as a dissolution mechanism (42, 43). In this case, substrate availability does not represent a substantial rate limiting factor because of the relatively low reaction rate and the abundancy of shale-associated OM. Therefore, seasonal temperature change represents the primary control of the variation in georespiration in agreement with the kinetic theory for recalcitrant OM (41).

Simulation results show that climate forcing has a significant impact on the carbonate weathering and pyrite oxidation that take place primarily below the soil horizon (Fig. 3 *F*–*H*). However, responses of these geochemical processes differ both spatially and temporally. In particular, dolomite dissolution is enhanced during periods combining large water infiltration events and hot moments in soil respiration. This increase is most pronounced within the depth interval [1 to 1.5] m (green dashed line in Fig. 3*F*; maximum rate of 1.54 mol C/m^3/y) and remains significant at depth >2 m (red dashed-dotted line in Fig. 3*F*; maximum rate of 0.19 mol C/m^3/y). Note that the model indicates that dolomite dissolution is inhibited from June to August, despite the large amount of CO_2 produced by root respiration (Fig. 3*D*). Moreover, the model shows that calcite precipitates at the expense of dolomite because of the lower solubility of calcite (i.e., negative dissolution rates in Fig. 3*G*. Such partial conversion of dolomite and/or ankerite to calcite has been reported in other carbonaceous shales (2, 6, 12) and is further evidenced at our site by the measured mineral concentration profiles showing a peak in calcite concentration below the dolomite weathering front (*SI Appendix*, Fig. S2). The average calcite precipitation rate is about one order of magnitude lower than that of dolomite dissolution, indicating that only a small fraction of the inorganic C is sequestered as secondary calcite (2.7×10^{-2} and 3.8×10^{-2} mol C/m^3/y within depth intervals [1 to 1.5] and [2 to 2.5] m, respectively). Furthermore, pyrite oxidation and subsequent iron precipitation are enhanced below 2 m during snowmelt because of the percolation of oxic water at depth (Fig. 3*H*). No significant oxidation of pyrite occurs at shallower depth because of the near complete removal of pyrite (*SI Appendix*, Fig. S2). The temporal trend in H^+ generation during sulfide mineral and iron oxidation mirrors the slight dissolution of carbonate minerals simulated within the depth interval [2 to 2.5] m (red dashed-dotted line in Fig. 3*F*) suggesting that pyrite oxidation drives a small part of carbonate weathering. In fact, when considering the stoichiometric ratio of two moles of protons consumed for one mole of mineral during dolomite dissolution, the maximum rate of proton release (0.44 mol H^+/m^3/y) corresponds to the maximum dolomite dissolution rate (0.19 mol C/m^3/y) within the depth interval [2 to 2.5] m. Finally, the model indicates that silicate and clay mineral dissolution/precipitation reactions have a minor impact on pH buffering at the timescale of our study due to the considerably lower reactivity of these minerals (i.e., average H^+ consumption by silicate reactions is 2.4×10^{-2} mol H^+/m^3/y).

Gas Diffusion and Thermodynamic Controls on Carbonate Weathering. Because dolomite weathering represents the dominant weathering process influencing the partitioning of C in the regolith, we explore the effects of water saturation and temperature variations on dolomite dissolution through their respective controls on gas diffusion and the thermodynamics of the carbonate system. Specifically, we carry out a series of simulations to quantify the impacts of i) gas diffusion variations induced by the dynamics of partially saturated flow, ii) temperature-controlled variations in dolomite solubility, and iii) temperature-controlled variations in $CO_{2(g)}$ solubility. Fig. 4 presents the simulated dolomite dissolution rates within the [1 to 1.5] m depth interval when assuming constant gas diffusion coefficients (Fig. 4*A*), dolomite equilibrium constants (Fig. 4*B*), and $CO_{2(g)}$ Henry's law coefficients (Fig. 4*C*). The results show that dolomite solubility and gas diffusion variations exert a substantial influence on carbonate weathering although they do not control the overall temporal trend of dolomite dissolution (Fig. 4 *A* and *B*). The model indicates that their effects are particularly pronounced in summer as the drier conditions favor the upward diffusion of $CO_{2(g)}$ to the atmosphere (agreement between the red dashed line and the black solid line in Fig. 4*A*) while the increasing temperature reduces dolomite solubility (agreement between the blue dashed line and black solid lines in Fig. 4*B*). Such conditions significantly limit the dissolution of dolomite after snowmelt. Furthermore, higher dolomite dissolution is predicted during large infiltration events when testing lower gas diffusion (peaks in blue dashed line compared to black solid line in Fig. 4*A*) because gas transport is most limited at the end of the snowmelt period when water saturation is highest (Fig. 3*A*). Finally, Fig. 4*C* shows that variations in $CO_{2(g)}$ solubility have a negligible influence on dolomite dissolution since all simulation results agree well with the calibrated model.

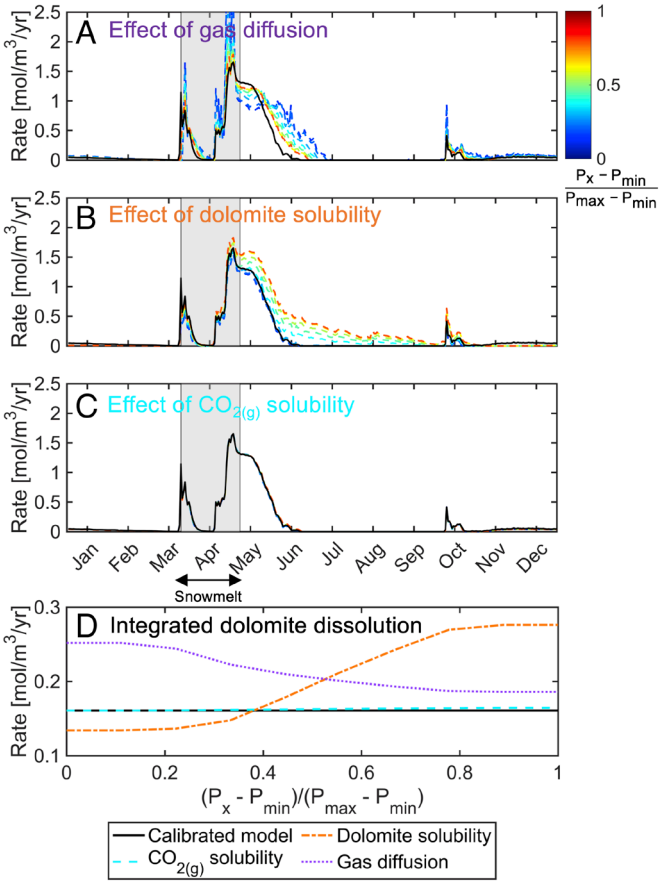

Fig. 4. Influence of gas diffusion and thermodynamic controls on dolomite dissolution. (*A*–*C*) Temporal evolution of the average dolomite dissolution rate within the [1 to 1.5] m depth interval predicted by the calibrated model (black solid line) and by the additional simulations exploring the parameter ranges (colored dashed lines). These simulations were performed by fixing (*A*) the effective gas diffusion coefficient, (*B*) the equilibrium constant of dolomite, or (*C*) the Henry's law constant of $CO_{2(g)}$ to values encompassing the ranges of effective parameter values used in the calibrated model (i.e., in the calibrated model, these parameters vary because they are function of temperature and water saturation). Simulations were repeated by changing one-by-one the parameter values using evenly spaced quantiles until the effective parameter ranges were fully explored. A total of 10 model runs were performed for each parameter. Units indicated in the color bar refer to the normalized tested parameter value P_x (P_{min} and P_{max} are the minimum and maximum value of the parameter range). (*D*) Variations in integrated dolomite dissolution simulated when parameters are varied within the explored range of values. Parameter values applied in these simulations are reported in *SI Appendix*.

In order to allow a quantitative comparison between the effects of dolomite solubility and that of gas diffusion variations, Fig. 4*D* summarizes the change in total dolomite dissolution when dolomite solubility and gas diffusion are varied within range used in the calibrated model. The results indicate that the variations in dolomite solubility caused by temperature variations have a stronger effect on dolomite dissolution than that of transient change in gas diffusion. In fact, the range of simulated dolomite dissolution is [0.02 to 0.23] mol/m^3/y when varying the equilibrium constant of dolomite, whereas this range is narrower in the case of gas diffusion (i.e., [0.12 to 0.20] mol/m^3/y).

Model-Based Interpretation of Carbon Flux Partitioning. By mathematically describing the carbon dynamics over the vertical extent of the regolith and across multiple phases (water, gas, solid) and by explicitly accounting for the effects of climatic forcing and the spatial distribution of the physico-chemical properties (i.e., mineral concentration, rooting depth, microbial biomass, water content), our modeling approach makes it possible to quantitatively discriminate the effects of individual biogeochemical processes on the C hydrogeochemical fluxes (25). Fig. 5 presents a comprehensive analysis of the C fluxes by displaying the biogeochemical budget of carbon (Fig. 5*A*), the monthly partitioning of inorganic carbon (Fig. 5*B*), and the individual contribution of biogeochemical processes to the DIC exports (Fig. 5*C*). Our results highlight the importance of seasonal shifts in key pathways induced by climate forcing as well as the connections between soil respiration and carbonate weathering in controlling the C partitioning between the atmosphere and the subsurface.

The biogeochemical budget of carbon presented in Fig. 5*A* shows that dissolved organic carbon (DOC) is derived primarily from the release of soil OM to the aqueous phase (93%, 334 mol C/m^2/y) and that leaching of litter OM represents a secondary but significant contribution to DOC (6%, 20.5 mol C/m^2/y). In contrast, shale-associated OM does not significantly contribute to the DOC fluxes (<1%, 3.41 mol C/m^2/y). Furthermore, while biomass growth retains most of the organic carbon (>90%), the high rate of soil heterotrophic respiration results in low exports of soil-derived DOC to the groundwater (~0.1 mol C/m^2/y).

Despite the low fraction of DOC being mineralized, soil respiration represents the primary mobilization pathway of inorganic carbon in the form of CO_2 (Fig. 5 *A* and *B*) with significantly higher contribution from heterotrophic respiration than root respiration since heterotrophic respiration persists during winter (21.7 and 13.7 mol C/m^2/y, respectively). In particular, Fig. 5*B* shows that the contribution of heterotrophic respiration is highest in spring due to the effect of snowmelt. Indeed, from April to June, heterotrophic respiration mobilizes 56% of the total inorganic carbon with a maximum attained in May (35 mol C/m^2/y). In comparison, the contribution of root respiration to inorganic carbon is maximum during the growing season, exceeding by two-fold that of heterotrophic respiration in early summer (47 and 40 mol C/m^2/y in June and July, respectively). Nearly all inorganic carbon mobilized by soil respiration is emitted to the atmosphere as $CO_{2(g)}$ emissions (97%, 34.3 mol C/m^2/y). In particular, Fig. 5*B* shows that the entire soil $CO_{2(g)}$ flux is well explained by the sum of root respiration and heterotrophic respiration. $CO_{2(g)}$ emissions are highest between snowmelt and the growing season (71 mol/m^2/y in June) and remain large during summer. In particular, large summer $CO_{2(g)}$ flux is favored by the proximity of the root zone with the soil surface and by the drier conditions maximizing gas diffusion. In fall and winter, root respiration ceases because of plant dormancy, whereas heterotrophic respiration is maintained leading to minimum soil $CO_{2(g)}$ production.

Although weathering reactions have a minor influence on the CO_2 flux between the soil and the atmosphere, they are important because they control the DIC exports (11) and regulate the global C cycling on a longer timescale (20). Here, we calculate that the flux of DIC mobilized via dolomite dissolution (0.73 mol C/m^2/y) is about 500 times lower than the total $CO_{2(g)}$ emissions, but this flux represents a significant fraction (63%) of the DIC exports to the groundwater (1.18 mol C/m^2/y; Fig. 5*A*). Results presented in Fig. 5*D* underscore the critical role of carbonate weathering for the transfer of inorganic carbon from the soil to the subsurface as the model predicts a 93% decrease in DIC exports when carbonate mineral dissolution is not considered (white dashed line compared to the back solid line in Fig. 5*C*). Interestingly, this fraction is higher than the net contribution of dolomite dissolution to DIC calculated in the biogeochemical budget (Fig. 5*A*). Such a difference underpins the importance of carbonate alkalinity in promoting the transfer of soil CO_2 to the saturated zone (here, 30%) by limiting the mass transfer of carbon from the aqueous to the gas

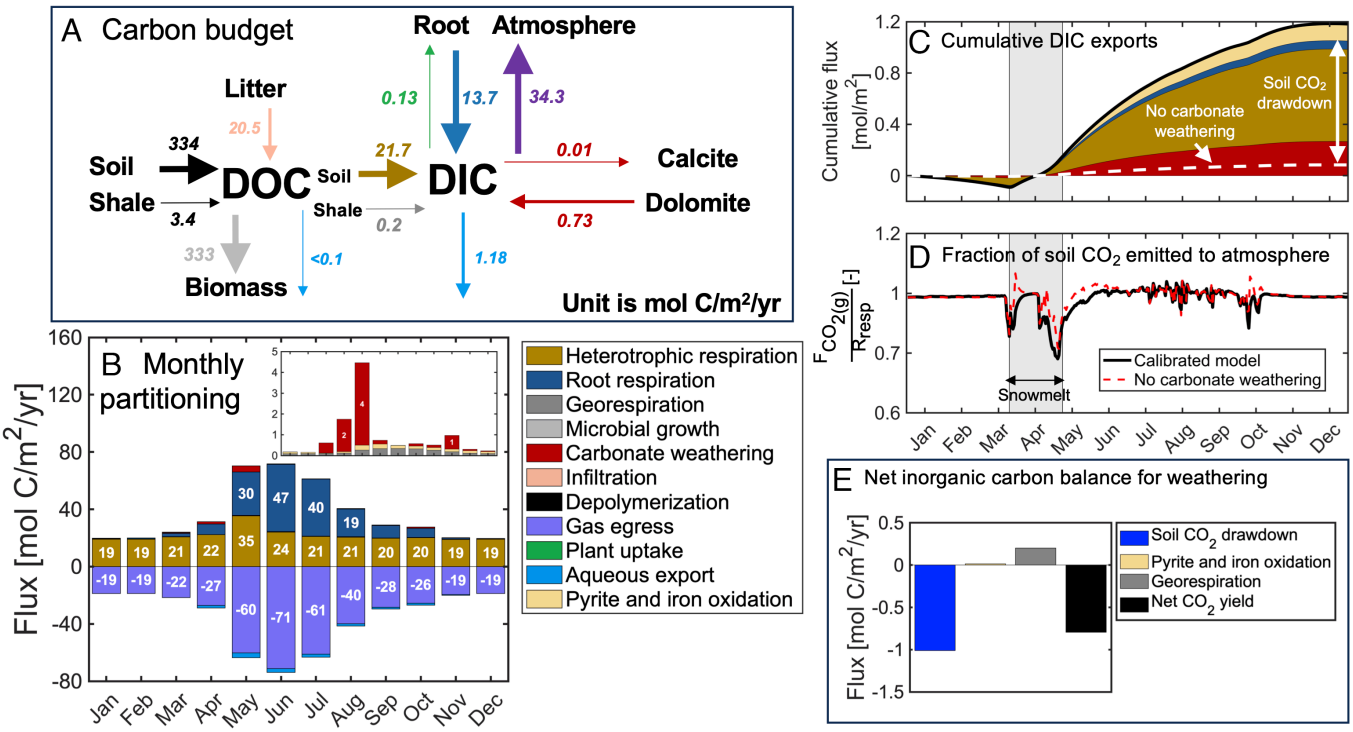

Fig. 5. Model-based interpretation of carbon fluxes partitioning in the regolith. (*A*) Annual biogeochemical budgets of carbon calculated based on the physics-based numerical simulations. Here, depolymerization refers to the mobilization of DOM from solid organic matter (SOM). (*B*) Monthly individual contributions of the key mechanisms controlling the mobilization, transport, and sequestration of inorganic carbon. In this panel, positive fluxes indicate mobilization pathways, negative fluxes indicate exports via gas emissions and aqueous exports, and white numbers indicate the total contribution of each pathway for a given month [mol C/m^2/y]. The zoom-in diagram shows the contribution of weathering processes including i) carbonate weathering, ii) georespiration, and iii) pyrite and iron oxidation. Contribution of pyrite and iron oxidation (in yellow) reflects how much inorganic carbon is mobilized from carbonate dissolution driven by the protons generated during the oxidation reactions. (*C*) Individual contributions of the biogeochemical processes to the DIC exports. These contributions were quantified using the calibrated model and discarding one-by-one the biogeochemical processes. The contribution of carbonate weathering was calculated based on a simulation in which only carbonate reactions were included. The white dashed line was computed by running the calibrated model without including the carbonate mineral reactions. (*D*) Temporal evolution of the ratio between $CO_{2(g)}$ flux at the soil/atmosphere interface ($F_{CO_{2(g)}}$) and mobilization rate of biogenic CO_2 (R_{resp}). This ratio is equivalent to the ARQ but, in this case, it accounts for both root respiration as well as microbial reactions as a source of CO_2. (*E*) Net inorganic carbon balance associated with weathering reactions. Soil CO_2 drawdown was calculated by subtracting the contribution of pyrite oxidation to the DIC exports. Net CO_2 yield was calculated as the sum of CO_2 drawdown (negative contribution) and CO_2 produced by weathering reactions (i.e., pyrite oxidation and georespiration; positive contribution).

phase, in agreement with the results of Hodges et al. (9). DIC mobilization from dolomite dissolution shows strong seasonal variations characterized by a sharp peak during snowmelt ([1.6 to 4.2] mol C/m^2/y; Fig. 5*B*). In comparison, the model indicates that calcite precipitation does not represent a substantial sink for inorganic carbon (~0.01 mol C/m^3/y).

Regarding the impact of oxidative weathering, the simulated amount of CO_2 generated by georespiration is significantly lower (~0.2 mol C/m^2/y) than the total DIC released through dolomite dissolution (Fig. 5*A*). Nonetheless, the model shows that the CO_2 flux associated with georespiration can exceed the carbonate weathering contribution between May and September due to warmer conditions and the absence of large water infiltration events (~0.3 mol C/m^2/y; Fig. 5*B*). In order to assess the impact of pyrite and ferrous iron oxidation on the C partitioning through the release of protons (i.e., together these processes generate a total of 2.31×10^{-1} mol H$^+$/m^2/y), we ran an additional simulation in which these oxidation reactions were discarded. Results show that pyrite and ferrous iron oxidation contribute only to 0.07% (2.4×10^{-2}) of the total $CO_{2(g)}$ emissions, whereas they are responsible for 11% of the total DIC exports (Fig. 5*C*). These fluxes indicate that the weathering of carbonates at depth effectively buffers the acidity derived from the oxidation of pyrite and, therefore, limits the mass transfer of inorganic C from aqueous to gas phase. Using a similar approach for assessing the influence of silicate and clay, we calculate that reactions associated with these minerals (Table 1) only consume ~8×10^{-2} mol H$^+$/m^2/y and therefore play a minor role for the carbon fluxes at the timescale of this study (<0.002% decrease in CO_2 egress when silicate and clay reactions are included).

Discussion

Connection between Soil Respiration and Shale Weathering. While the influence of soil respiration on carbonate weathering has been documented (e.g., refs. 6–10), a mechanistic description of their coupling under transient conditions and a rigorous analysis of the effects of climate factors have been missing. Our model-based interpretation sheds light on the pivotal role of climate forcing in governing the partitioning of C fluxes during the weathering of shale as it determines the degree of biogeochemical coupling between the rapid carbon cycling in soil and the long-term fluxes associated with weathering. In particular, our analysis shows that infiltration events and temporal variation in water saturation control the connection between soil heterotrophic respiration and carbonate weathering by stimulating a cascade of biogeochemical and multiphase transport mechanisms. First, higher accessibility of labile OM to microorganisms during soil rewetting enhances heterotrophic respiration and leads to the rapid mobilization of biogenic CO_2. Second, the percolation of water promotes the downward penetration of carbonic acid and the reaction with carbonates. Finally, the time-dependent variations in water saturation determine the rate of $CO_{2(g)}$

Table 1. Kinetic aqueous reactions and mineral dissolution/precipitation reactions defined in the model

	Aqueous reactions
Processes	Reaction stoichiometry
Aerobic respiration	$(CH_2O)(NH_3)_x + O_2 = H^+ + HCO_3^- + xNH_3$
Ferrous iron oxidation	$Fe^{2+} + 0.25O_2 + H^+ = Fe^{3+} + 0.5H_2O$
	Microbial biomass
Growth	$(CH_2O)(NH_3)_x + (y-x)NH_4^+ = B + (y-x)H^+$
	Mineral phase dissolution/precipitation reactions
Minerals	Reaction stoichiometry
Dolomite	$MgCa(CO_3)_2 + 2H^+ = Mg^{2+} + Ca^{2+} + 2HCO_3^-$
Albite	$NaAlSi_3O_8 + 4H^+ + 4H_2O = Al^{3+} + Na^+ + 3H_4SiO_4$
Chlorite*	$Fe_5Al_2Si_3O_{10}(OH)_8 + 16H^+ = 5Fe^{2+} + 2Al^{3+} + 3H_4SiO_4 + 6H_2O$
Quartz	$SiO_2 + 2H_2O = H_4SiO_4$
Pyrite (oxygen)	$FeS_2 + 3.5O_2 + H_2O = Fe^{2+} + 2SO_4^{2-} + 2H^+$
Pyrite (ferric iron)	$FeS_2 + 14Fe^{3+} + 8H_2O = 15Fe^{2+} + 2SO_4^{2-} + 16H^+$
Goethite	$Fe^{3+} + 2H_2O = FeOOH + 3H^+$
Calcite	$Ca^{2+} + CO_3^{2-} = CaCO_3$
Illite†	$K_{0.85}Al_{2.35}Fe_{0.25}Si_{3.4}O_{10}(OH)_2 + 8.4H^+ + 1.6H_2O = 2.35Al^{3+} + 3.4H_4SiO_4 + 0.85K^+ + 0.25Fe^{2+}$
	Organo-mineral interactions
Soil-derived OM	$SOM_1 \rightarrow DOM_1$
Shale-associated OM	$SOM_2 \rightarrow DOM_2$

*The stoichiometry of chamosite was adopted based on the XRD analyses showing a Fe^{2+}-rich chlorite.
†The stoichiometry provided by (44) was adopted based on the XRD analyses showing an Al^{3+}-rich illite.
The reactions involving DOM, defined with the general stoichiometry $(CH_2O)(NH_3)_x$, were included for both soil-derived and shale-associated organic matter with x the N:C ratios equal to 0.07 and 0.1, respectively. y is the N/C ratio of biomass and equal to 0.07.

egress to the atmosphere and consequently the effectiveness of the reaction between carbonic acid and carbonates. At our site, we find that this transfer of biogenic CO_2 from the soil horizon to the subsurface is seasonally favored during snowmelt as it represents the largest infiltration event at the year scale. In fact, 69% of the total DIC exports to the subsurface occur from April to July (1.96 mol C/m^2/y, SD: 1.43), while heterotrophic respiration explains 61% of the yearly DIC exports (Fig. 5*C*). The increase in DIC and base cations fluxes observed in streams during spring snowmelt (14, 22, 31) suggests that this mechanism is particularly important for the seasonal exports of solutes in snow-covered watersheds. In comparison, the model shows that root respiration does not significantly contribute to the DIC exports at our site (6%, Fig. 5*C*). In fact, the relatively dry conditions that prevail in the shallow root zone (20 cm) and the dominance of root respiration during periods of lower water infiltration results in the rapid egress via gas diffusion of root-derived $CO_{2(g)}$ to the atmosphere. Thus, such conditions minimize the effect of root respiration on carbonate weathering.

Our estimate of the total CO_2 drawdown is equivalent to about 3% of soil respiration CO_2 inputs and is consistent with mass balance calculations based on solute exports (6, 7, 45). However, this fraction is significantly lower than previous calculations based on the aerobic respiration quotient (ARQ) and snapshots of $O_{2(g)}$ and $CO_{2(g)}$ concentration distribution at the soil/atmosphere interface (7–9, 46). Unlike the ARQ, our physics-based model considers the complex fluid phase distribution (water and gas), which is crucial for accurately describing the transport behavior of gas components under transient conditions (17). In particular, the model accounts for the local degree of water saturation to simulate the rate of gas diffusion at a given depth (*SI Appendix*). As displayed in Fig. 5*D*, the model allows us to directly compare the $CO_{2(g)}$ flux from the soil to the atmosphere ($F_{CO_{2(g)}}$) and the rate of CO_2 release from biological processes (R_{resp}). A sharp decrease in $F_{CO_{2(g)}} / R_{resp}$ is simulated during large infiltration events reaching a minimum of 0.73 during snowmelt. While this result has been interpreted as the occurrence of significant entrapment of CO_2 in the subsurface as a result of the coupling between aqueous transport and geochemical reactions (e.g., ref. 22), the low fraction of $CO_{2(g)}$ effectively transferred to the subsurface simulated by our model argues against this hypothesis. Instead, the model shows that the difference between $F_{CO_{2(g)}}$ and R_{resp} is primarily controlled by mass-transfer limitations taking place under transient hydrological conditions. In particular, the egress of biogenic $CO_{2(g)}$ is temporarily limited during snowmelt due to the high water content that hinders gas diffusion, while hot moments in heterotrophic respiration generate large amounts of CO_2. Subsequent to these transient events, $CO_{2(g)}$ diffusion increases as water saturation recedes. Such transient propagation of gaseous species leads to a lag between the production of biogenic CO_2 and its release to the atmosphere and highlights the need to explicitly account for transient change in physical conditions when assessing the effects of climate forcing on soil CO_2 drawdown.

Implications for the Carbon Budget of Shale Weathering. Since soil CO_2 drawdown dominates the weathering C fluxes via the coupling between heterotrophic respiration and dolomite dissolution in comparison to oxidation reactions (pyrite and shale-associated OM), we find that the chemical weathering of shale acts as a net sink of CO_2 under the specific conditions of our site (Fig. 5*E*). In particular, the deep pyrite weathering front and the consumption of O_2 by heterotrophic respiration in the soil layer lead to a relatively limited impact of pyrite oxidation on the carbon balance. In comparison, analysis of concentration-discharge patterns for riverine solutes has shown that a significant fraction

of carbonate weathering is driven by sulfuric acid under base flow conditions at the East River (22). These contrasting findings suggest that pyrite oxidation may play a more important role for the C partitioning at a larger scale compared to that calculated at the lower slope position of our field site. For instance, more intense oxidative weathering of pyrite may occur as a result of deep subsurface flow paths (22, 40) as well as the larger extent of the unsaturated zone (47) and/or higher erosion rates under ridge tops (23, 48). In particular, rapid erosion rates in mountainous environments typically result in positive contribution of shale weathering to CO_2 atmospheric levels. In fact, such conditions lead to exhumation of fresh petrogenic OM and sulfide minerals to the capillary fringe thereby promoting intense oxidation of these solid phases (5, 15, 16, 23). Heterogeneous vegetation cover could further contribute to shaping a different carbon balance at a larger scale (11) as vegetation influences soil heterotrophic respiration and can enhance CO_2 drawdown through root respiration in areas where rooting depths extend to the zone of active weathering (10, 45, 49, 50). Understanding the aggregated controls shaping hydrogeochemical export and the partitioning of carbon at a larger scale will thus require upscaling our modeling framework (28, 51) to account for deep flow paths as well as key functional zones characterized by different external factors, biogeochemical and hydrological conditions, and/or vegetation species.

Given the critical role of georespiration for the net carbon balance of sedimentary rock weathering (20), significant effort has been devoted to quantify the rate of petrogenic OM oxidation in the laboratory (21, 42) and in the field (1, 4, 6, 15, 16, 21, 40). In this study, we parameterized the rate of georespiration based on a recent study which utilized riverine dissolved rhenium concentration time series to quantify the flux of petrogenic OM oxidation at the East River (40). Because this flux is representative of the catchment scale aggregated response, it may include the contribution of multiple functional zones where the intensity of georespiration differs as a result of spatially heterogeneous erosion regime (e.g., decreasing from ridges to valley floor) (23, 48). In particular, we note that this flux (1×10^{-1} mol C/m^2/y) is intermediate between that measured in low eroding shales covered with a soil layer (i.e., 1.3×10^{-3} and 4.5×10^{-2} mol C/m^2/y for Silurian and Cretaceous shales, respectively) (4, 6) and that measured in outcrops where relatively well preserved petrogenic OM are exposed to atmospheric conditions (6.75 to 60 mol C/m^2/y) (15, 16). Future integration of radiocarbon data in our modeling framework will support the refinement of the CO_2 flux associated with georespiration for the local conditions under consideration (4, 21, 52).

Finally, considering the strong controls of external forcing on subsurface biogeochemical processes, climate change is expected to alter the carbon fluxes associated with shale weathering. In particular, our results suggest that future no-snow conditions (53) will lower the transport of soil CO_2 to the carbonate weathering front, whereas higher temperature will lead to lower carbonate solubility (Fig. 4) and an increase in petrogenic OM oxidation (15, 16). Moreover, increase in sulfide mineral oxidation has been observed as a result of reduced groundwater recharge and declining water tables (19). This suggests that climate warming could promote a reduction in soil CO_2 consumption by carbonate weathering and an enhancement in CO_2 release via oxidative weathering. However, the impact of climate change on the net carbon balance cannot easily be extrapolated from the present conditions due to the complex interactions and feedback between evolving processes that add additional degrees of freedom beyond what is considered here. In particular, changes in net primary productivity and soil respiration induced by warming and higher atmospheric CO_2 concentration (37, 54) are known to influence the weathering processes (28). The integration of additional model components explicitly describing the evolution of soil biological processes driven by climate change and their impacts on hydrological and biogeochemical conditions in physics-based models will provide the capabilities to explore the long-term interplay between climate and rock weathering.

Methods

Field Site. The study area is located in the Rocky Mountains within the East River watershed, near Gothic, Colorado (*SI Appendix*, Fig. S1). The East River watershed is used as a community testbed to gain insights into the key hydrological and biogeochemical processes governing water/solutes export in mountainous watersheds. It is part of the Watershed Function scientific focus area (SFA) led by Lawrence Berkeley National Laboratory (29). In this study, we consider a 140 m hillslope transect exposed northeast with an average slope of 19%, located within altitudes ranging between 2,750 m and 2,800 m, and draining into a floodplain adjacent to the East River (*SI Appendix*, Fig. S1*A*) (33, 55). The shale primarily consists of quartz (40.22 wt%), clay minerals (36.3 wt% in total) composed of chlorite and illite, and carbonate minerals that consist of dolomite (13.70 wt%) and a minor amount of calcite (1.23 wt%). Pyrite and shale-associated OM represent low fractions of the total mineral assemblage (0.90 wt% and 1.25 wt%, respectively; *SI Appendix*, Table S1). The plant community at the field site is composed of perennial bunchgrasses (e.g., *Festuca arizonica*), forbs (e.g., *Lupinus spp.*, *Potentilla gracilis*, *Veratrum californicum*), and shrubs (*Artemisia tridentata*) representative of the dominant land cover of the Upper Colorado River Basin (56). The climate is continental, subarctic characterized by long cold winters and short cool summers with average annual air temperature, precipitation, and evapotranspiration (ET) equal to 3 °C, 700 mm, and 500 mm respectively. About 70% of the precipitation occurs as snow fall between October and May. Rising temperature in spring drives snowmelt, which leads to an abrupt rise of the water table followed by its progressive decline over the year (Fig. 3*A*). Summer is characterized by an arid climate and intermittent monsoonal rain events which do not significantly contribute to groundwater recharge due to the strong ET prevailing during this period. Three observation wells (PLM1, PLM2, and PLM3) were drilled in 2016 to a depth of 10 m along the transect using a track-mounted drill rig and a 0.14 m diameter ODEX drilling bit. The wells are equipped with suction lysimeters and pore gas samplers to carry out vertically discrete pore water and gas sampling, respectively; pressure transducers to perform daily measurements of the water table [AquaTROLL 2000; except in PLM2 where the water table was determined from equilibrium pressure and moisture measurements (33)]; and temperature sensors. Details on solid and fluid sampling and analyses are provided in *SI Appendix*.

Modeling Approach and Numerical Implementation. This section summarizes the key features of the physics-based model. Technical details including the set of partial differential equations and model parameters are presented in *SI Appendix*.

Shale weathering and the associated biogeochemical reactions were simulated using the finite volume reactive transport code CrunchTope (57), which has recently been upgraded with the capability to calculate variably saturated flow using the Richards equations (58). The model builds on the modeling framework of Stolze et al. (3) with the addition of the following:

- The explicit description of root respiration and exudation;
- The release of soil DOM as a function of water saturation;
- Transient boundary conditions reproducing the water infiltration from rainfall and snowmelt as well as the evapotranspiration fluxes;
- Spatial and temporal variations in temperature and their impact on the biogeochemical reaction rates;
- The description of ion exchange reactions between the solid materials and the aqueous phase.

We assume vertical percolation of water since biogeochemical reactions controlling carbonate weathering dominate in the upper 2 m. Partially saturated flow was simulated by solving the Richards equation (58) using the van Genuchten–Mualem model (59, 60) for describing water retention and conductivity properties of the porous medium. Infiltration of meteoric water was simulated by defining a

flux boundary condition at the top of the model domain. Infiltration time series were implemented by combining precipitation measurements and snowpack drainage simulations that were performed with the snowmelt model ESCIMO.spread v2 (61). Evapotranspiration fluxes were calculated through land surface simulations considering local meteorological forcing data. Evaporation was assumed to only modify the water content without affecting the mass of solutes, whereas transpiration was assumed to affect both water and solutes over the rooting depth. Minimum water table depth was fixed by defining a constant pressure head condition at the bottom. The hydrogeophysical parameters (i.e., permeability, porosity, and van Genuchten parameters) were calibrated to reproduce the water infiltration flux as well as the transient distribution of liquid phase observed at the site. To account for the effect of seasonal temperature variations, we define depth-discretized temperature time series based on the continuous temperature measurements performed in the monitoring wells at different depths (*SI Appendix*, Fig. S6).

The model considers the advective-dispersive transport of solutes in the aqueous phase and the diffusive transport of chemical species in the gas phase. In particular, our simulations include 20 primary species (i.e., used for mass conservation transport equation; e.g., H^+), 26 secondary species in the aqueous phase (i.e., used for aqueous reactions and mineral transformation calculations; e.g., OH^-) as well as four species in the gas phase $O_{2(g)}$, $CO_{2(g)}$, $N_{2(g)}$, and $N_2O_{(g)}$. CrunchTope simulates the chemical reactions between primary and secondary species assuming equilibrium relationships. Primary species and secondary reactions are listed in *SI Appendix*, Table S2. The mass transfer of chemical species between the aqueous and gas phase was described with Henry's law. Equilibrium constants controlling aqueous speciation and Henry's law coefficients at specific temperatures were from the thermodynamic database Thermoddem (62) and are summarized in *SI Appendix*, Table S2. The activity coefficients of the aqueous species were calculated based on the extended Debye–Hückel equations (63). Gas exchange between the subsurface and the atmosphere was simulated by defining a Dirichlet boundary condition with fixed partial pressure of reactive gases composing the atmosphere at the altitude of the field site (i.e., $pO_2 = 1.68 \times 10^{-1}$ bar, $pN_2 = 6.24 \times 10^{-1}$ bar, and $pCO_2 = 3.17 \times 10^{-4}$ bar).

The domain was discretized into 10 cm grid cells. Model spin-up was run for 10 y in order to ensure representative flow and hydrochemical conditions prior to running the 1 − y simulation considered in this study.

Biogeochemical Reaction Network. The model describes a series of kinetically controlled biological processes and abiotic geochemical reactions that are influenced by the local hydrochemical conditions, the temporal change in temperature and water saturation, and the exchange of gases between the subsurface and the atmosphere. In particular, the biological processes include a series of microbially mediated reactions and the release of CO_2 and exudates from the root during the growing season. The reaction network is composed of i) the aerobic respiration of DOM, ii) the oxidative dissolution of the sulfide mineral pyrite, iii) the oxidation of ferrous iron to ferric iron and the precipitation of iron and oxide, iv) the dissolution/precipitation of carbonate, silicate, and clay minerals. Two types of OM with different reactivities were defined in the model: a petrogenic shale-associated OM present in the bedrock and a soil-derived OM dominant in the top soil. The latter accounts for i) DOM leached from litter, ii) DOM released from SOM in soil during rewetting, and iii) root exudates. The model explicitly considers the growth and decay of microbial biomass (64). The list of kinetically controlled reactions integrated into the model is provided in Table 1. The model accounts for the effect of temperature on the biogeochemical reactions by using Arrhenius-type kinetic rate expressions and by accounting for the temperature dependency of mineral and gas solubility as well as aqueous speciation (i.e., using temperature-dependent equilibrium constants and Henry's law coefficients). In particular, equilibrium constants controlling the mineral reactions, partitioning of chemical species between the water and gas phases, and aqueous speciation are updated as a function of temperature using polynomial fitting. Finally, the model simulates ion exchange reactions by defining mass action expressions with associated equilibrium constants and assuming local equilibrium conditions. The cation exchange capacity (CEC) of the solid materials was calculated by accounting for the content of illite, chlorite, and organic matter and validated against CEC measurements performed at our field site. The reactions between the exchanger and the aqueous phase include the exchange of Na^+, K^+, Ca^{2+}, and Mg^{2+}. Our simulations indicate that ion exchange reactions do not influence the carbon fluxes and concentrations of base cations and therefore are not discussed further in this study.

Data, Materials, and Software Availability. All study data are included in the article and/or *SI Appendix*.

ACKNOWLEDGMENTS. This work was supported by the Watershed Function Science Focus Area project at Lawrence Berkeley National Laboratory funded by the US Department of Energy, Office of Science, Biological and Environmental Research under Contract No. DE-AC02-05CH11231. The US Government retains, and the publisher, by accepting the article for publication, acknowledges, that the US Government retains a nonexclusive, paid-up, irrevocable, world-wide license to publish or reproduce the published form of this manuscript, or allow others to do so, for US Government purposes. We thank Robert Hilton and two additional reviewers for their constructive criticism that improved the quality of the manuscript.

1. S. Petsch, K. Edwards, T. Eglington, Microbial transformations of organic matter in black shales and implications for global biogeochemical cycles. *Palaeo* **219**, 157–170 (2005).
2. X. Gu *et al.*, Seismic refraction tracks porosity generation and possible CO_2 production at depth under a headwater catchment. *Proc. Natl. Acad. Sci. U.S.A.* **117**, 18991–18997 (2020).
3. L. Stolze *et al.*, Aerobic respiration controls on shale weathering. *Geochim. Cosmochim. Acta* **340**, 172–188 (2023).
4. K. Keller, D. Bacon, Soil respiration and georespiration distinguished by transport analyses of vadose CO_2, $^{13}CO_2$, and $^{14}CO_2$. *Glob. Biogeochem. Cycles* **12**, 361–372 (1998).
5. J. Zondervan *et al.*, Rock organic carbon oxidation CO_2 release offsets silicate weathering sink. *Nature* **623**, 329–333 (2023).
6. L. Jin *et al.*, The CO_2 consumption potential during gray shale weathering: Insights from the evolution of carbon isotopes in the Susquehanna Shale Hills critical zone observatory. *Geochim. Cosmochim. Acta* **142**, 260–280 (2014).
7. Y. Olshansky *et al.*, Soil fluid biogeochemical response to climatic events. *J. Geophys. Res. Biogeosci.* **124**, 2866–2882 (2019).
8. E. Sànchez-Cañete, G. Barron-Gafford, J. Chorover, A considerable fraction of soil-respired CO_2 is not emitted directly to the atmosphere. *Nat. Sci. Rep.* **8**, 1–10 (2018).
9. C. Hodges *et al.*, Soil carbon dioxide flux partitioning in a calcareous watershed with agricultural impacts. *J. Geophys. Res. Biogeosci.* **126**, 1–21 (2021).
10. A. Tune *et al.*, Carbon dioxide production in bedrock beneath soils substantially contributes to forest carbon cycling. *J. Geophys. Res. Biogeosci.* **125**, 1–13 (2020).
11. J. Gaillardet, D. Calmels, G. Romero-Mujalli, E. Zakharova, J. Hartmann, Global climate control on carbonate weathering intensity. *Chem. Geol.* **527**, 118762 (2018).
12. K. Keller, Carbon exports from terrestrial ecosystems: A critical-zone framework. *Ecosystems* **22**, 1691–1705 (2019).
13. M. Carbone *et al.*, Seasonal and episodic moisture controls on plant and microbial contributions to soil respiration. *Oecologia* **167**, 265–278 (2011).
14. B. Arora *et al.*, Influence of hydrological, biogeochemical and temperature transients on subsurface carbon fluxes in a flood plain environment. *Biogeochem* **127**, 367–396 (2016).
15. G. Soulet *et al.*, Temperature control on CO_2 emissions from the weathering of sedimentary rocks. *Nat. Geosci.* **14**, 665–671 (2021).
16. T. Roylands *et al.*, Capturing the short-term variability of carbon dioxide emissions from sedimentary rock weathering in a remote mountainous catchment, New Zealand. *Chem. Geol.* **608**, 1–15 (2022).
17. N. Ahmadi *et al.*, Oxygen propagation fronts in porous media under evaporative conditions at the soil/atmosphere interface: Lab-scale experiments and model-based interpretation. *Water Resour. Res.* **58**, 1–20 (2022).
18. L. Li *et al.*, River water quality shaped by land–river connectivity in a changing climate. *Nat. Climate Change* **14**, 225–237 (2024).
19. A. Manning, T. Petach, R. Runkel, D. Mcknight, Climate-driven increases in stream metal concentrations in mineralized watersheds throughout the Colorado Rocky Mountains, USA. *Water Resour. Res.* **60**, 1–19 (2024).
20. R. Hilton, J. West, Mountains, erosion and the carbon cycle. *Nat. Rev. Earth Env.* **1**, 284–299 (2020).
21. A. Tune, J. Druhan, C. Lawrence, D. Rempe, Deep root activity overprints weathering of petrogenic organic carbon. *Earth Planet. Sci. Lett.* **607**, 1–12 (2023).
22. M. Winnick *et al.*, Snowmelt controls on concentration-discharge relationships and the balance of oxidative and acid–base weathering fluxes in an alpine catchment, East River, Colorado. *Water Resour. Res.* **53**, 2507–2523 (2017).
23. A. Bufe *et al.*, Co-variation of silicate, carbonate and sulfide weathering drives CO_2 release with erosion. *Nat. Geosci.* **14**, 211–216 (2021).
24. C. Steefel, Reactive transport at the crossroads. *Rev. Min. Geochem.* **85**, 1–26 (2019).
25. Y. Wang, P. Van Cappellen, A multicomponent reactive transport model of early diagenesis: Application to redox cycling in coastal marine sediments. *Geochim. Cosmochim. Acta* **60**, 2993–3014 (1996).
26. K. Maher, C. Chamberlain, Hydrologic regulation of chemical weathering and the geologic carbon cycle. *Science* **343**, 1502–1504 (2014).
27. H. Wen *et al.*, From soils to streams: Connecting terrestrial carbon transformation, chemical weathering, and solute export across hydrological regimes. *Water Resour. Res.* **58**, 1–26 (2022).

28. E. Beaulieu, Y. Goddéris, Y. Donnadieu, D. Labat, C. Roelandt, High sensitivity of the continental-weathering carbon dioxide sink to future climate change. *Nat. Climate Change* **2**, 346–349 (2012).
29. S. Hubbard *et al.*, The East River, Colorado, Watershed: A mountanous community testbed for improving predictive understanding of multiscale hydrological-biogeochemical dynamics. *Vadoze Zone J.* **17**, 1–25 (2018).
30. B. Arora *et al.*, Differential C-Q analysis: A new approach to inferring lateral transport and hydrologic transients within multiple reaches of a mountainous headwater catchment. *Front. Water* **2**, 1–20 (2020).
31. R. Carroll *et al.*, Factors controlling seasonal groundwater and solute flux from snow-dominated basins. *Water Critic. Zone* **32**, 2187–2202 (2018).
32. P. Fox *et al.*, Shale as a source of organic carbon in floodplain sediments of a mountainous watershed. *Water Resour. Res.* **125**, 1–21 (2020).
33. J. Wan *et al.*, Bedrock weathering contributes to subsurface reactive nitrogen and nitrous oxide emissions. *Nat. Geosci.* **14**, 217–224 (2021).
34. P. Sorensen *et al.*, The snowmelt niche differentiates three microbial life strategies that influence soil nitrogen availability during and after winter. *Front. Microbiol.* **11**, 1–18 (2020).
35. B. Arora *et al.*, "Hot spots and hot moments in the critical zone: Identification of and incorporation into reactive transport models" in *Biogeochemistry of the Critical Zone*, A. S. Wymore, W. H. Yang, W. L. Silver, W. H. McDowell, J. Chorover, Eds. (Springer, 2022), pp. 9–47.
36. H. Birch, The effect of soil drying on humus decomposition and nitrogen availability. *Plant Soil* **10**, 9–31 (1958).
37. P. Brooks, M. Williams, Snowpack controls on nitrogen cycling and export in seasonally snow-covered catchments. *Hydrol. Processes* **13**, 2177–2190 (1999).
38. O. Rindt *et al.*, Biogeochemical dynamics during snowmelt and in summer in the Alps. *Biogeochem* **162**, 257–266 (2023).
39. S. Manzoni, F. Moyano, T. Kätterer, J. Schimel, Modeling coupled enzymatic and solute transport controls on decomposition in drying soils. *Soil Biol. Biochem.* **95**, 275–287 (2016).
40. R. Hilton *et al.*, Concentration-discharge relationships of dissolved rhenium in alpine catchements reveal its use as a tracer of oxidative weathering. *Water Resour. Res.* **57**, 1–18 (2021).
41. E. Davidson, I. Janssens, Temperature sensitivity of soil carbon decomposition and feedbacks to climate change. *Nature* **440**, 165–173 (2006).
42. S. Chang, R. Berner, Humic substance formation via the oxidative weathering of coal. *Environ. Sci. Technol.* **32**, 2883–2886 (1998).
43. S. Schillawski, S. Petsch, Release of biodegradable dissolved organic matter from ancient sedimentary rocks. *Glob. Biogeochem. Cycles* **22**, 1–8 (2008).
44. Y. Goddéris *et al.*, Modelling weathering processes at the catchment scale: The WITCH numerical model. *Geochim. Cosmochim. Acta* **70**, 1128–1147 (2006).
45. D. Calmels, J. Gaillardet, L. Francois, Sensitivity of carbonate weathering to soil CO_2 production by biological activity along a temperate climate transect. *Chem. Geol.* **390**, 74–86 (2014).
46. A. Angert *et al.*, Using O_2 to study the relationships between soil CO_2 efflux and soil respiration. *Biogeosci* **12**, 2089–2099 (2015).
47. R. Liao *et al.*, Weathering of chlorite from grain to watershed: The role and distribution of oxidation reactions in the subsurface. *Geochim. Cosmochim. Acta* **333**, 284–307 (2022).
48. L. Ma *et al.*, Regolith production rates calculated with uranium-series isotopes at Susquehanna/Shale Hills Critical Zone Observatory. *Earth Planet. Sci. Lett.* **297**, 211–225 (2010).
49. H. Wen *et al.*, Deepening roots can enhance carbonate weathering by amplifying CO_2-rich recharge. *Biogeosci* **18**, 55–75 (2021).
50. E. Hasenmueller *et al.*, Weathering of rock to regolith: The activity of deep roots in bedrock fractures. *Geoderma* **300**, 11–31 (2017).
51. Z. Xu *et al.*, Understanding the hydrogeochemical response of mountainous watershed using integrated surface-subsurface flow and reactive transport modeling. *Water Resour. Res.* **58**, 1–23 (2022).
52. C. Steefel, J. Druhan, K. Maher, Modeling coupled chemical and isotopic equilibration rates. *Proced. Earth Planet. Sci.* **10**, 208–217 (2014).
53. E. Siirila-Woodburn *et al.*, A low-to-no snow future and its impacts on water resources in the western United States. *Nat. Rev. Earth Env.* **2**, 801–819 (2021).
54. S. Wenzel, P. Cox, V. Eyring, P. Friedlingstein, Projected land photosynthesis constrained by changes in the seasonal cycle of atmospheric CO_2. *Nat. Res. Lett.* **538**, 499–501 (2016).
55. T. Tokunaga *et al.*, Depth- and time-resolved distributions of snowmelt-driven hillslope subsurface flow and transport and their contributions to surface waters. *Water Resour. Res.* **55**, 9474–9499 (2019).
56. N. Falco *et al.*, Investigating microtopographic and soil controls on a mountainous meadow plant community using high-resolution remote sensing and surface geophysical data. *J. Geophys. Res.* **124**, 1618–1636 (2019).
57. C. Steefel *et al.*, Reactive transport codes for subsurface environmental simulation. *Comput. Geosci.* **19**, 445–478 (2015).
58. L. Richards, Capillary conduction of liquids through porous mediums. *J. Appl. Phys.* 318–333 (1931).
59. Y. Mualem, A new model for predicting the hydraulic conductivity of unsaturated porous media. *Water Resour. Res.* **12**, 513–522 (1976).
60. M. van Genuchten, A closed-formulation for predicting the hydraulic conductivity of unsaturated soils. *Soil Sci. Soc. Am. J.* **44**, 892–898 (1980).
61. T. Marke *et al.*, ESCIMO.spread (v2): Parameterization of a spreadsheet-based energy balance snow model for inside-canopy conditions. *Geosci. Model Dev.* **9**, 633–646 (2016).
62. P. Blanc *et al.*, Thermoddem: A geochemical database focused on low temperature water/rock interactions. *Appl. Geochem.* **27**, 2107–2116 (2012).
63. H. Helgeson, W. Murphy, P. Aagaard, Thermodynamic and kinetic constraints on reaction rates among minerals and aqueous solutions. II. Rate constants, effective surface area, and the hydrolysis of feldspar. *Geochim. Cosmochim. Acta* **48**, 2405–2432 (1984).
64. S. Molins, J. Greskowiak, C. Wanner, U. Mayer, A benchmark for microbially mediated chromium reduction under denitrifying conditions in a biostimulation column experiment. *Comput. Geosci.* **19**, 479–496 (2015).